J Oceanogr (2013) 69:619–630
DOI 10.1007/s10872-013-0198-0

ORIGINAL ARTICLE

The variability of internal tides in the Northern South China Sea

Barry B. Ma · Ren-Chieh Lien · Dong S. Ko

Received: 5 April 2013 / Revised: 30 June 2013 / Accepted: 11 August 2013 / Published online: 27 August 2013

Abstract An array of three bottom-mounted ADCP moorings was deployed on the prevailing propagation path of strong internal tides for nearly 1 year across the continental slope in the northern South China Sea. These velocity measurements are used to study the intra-annual variability of diurnal and semidiurnal internal tidal energy in the region. A numerical model, the Luzon Strait Ocean Nowcast/Forecast System developed at the U.S. Naval Research Laboratory that covers the northern South China Sea and the Kuroshio, is used to interpret the observed variation of internal tidal energy on the Dongsha slope. Internal tides are generated primarily at the two submarine ridges in the Luzon Strait. At the western ridge generation site, the westward energy flux of the diurnal internal tide is sensitive to the stratification and isopycnal slope associated with the Kuroshio. The horizontal shear at the Kuroshio front does not modify the propagation path of either diurnal or semidiurnal tides because the relative vorticity of the Kuroshio in Luzon Strait is not strong enough to increase the effective inertial frequency to the intrinsic frequency of the internal tides. The variation of internal tidal energy on the continental slope and Dongsha plateau can be attributed to the variation in tidal beam propagation in the northern South China Sea.

Keywords Internal tide · Horizontal kinetic energy · Energy flux · Kuroshio · South China Sea · Luzon Strait

B. B. Ma (✉) · R.-C. Lien
Applied Physics Laboratory, University of Washington, 1013 NE 40th Street, Seattle, WA 98105, USA
e-mail: barry@apl.uw.edu; barry@apl.washington.edu

D. S. Ko
Naval Research Laboratory, Stennis Space Center, 1 Stennis Space Ctr, MS 39529, USA

1 Introduction

The northern South China Sea (SCS) is the site of some of the most intense internal wave action in the world ocean. Internal waves are generated in the Luzon Strait (LS) primarily through the interaction of the barotropic tide with the two submarine ridges, Heng-Chun Ridge (western ridge) and Lan-Yu Ridge (eastern ridge, also known as Luzon Ridge or Luzon Island Arc; Fig. 1). The waves propagate westward toward the northern SCS and eastward toward the Pacific Ocean. Two categories of internal gravity waves, large-amplitude solitary-type waves of depression (solitons) and waves at or near tidal frequencies (internal tides), dominate the northern SCS (Duda et al. 2004; Ramp et al. 2004). Mooring measurements show that internal tides in the SCS have a strong fortnightly cycle (Duda et al. 2004; Lee et al. 2012). The diurnal tide is stronger than the semidiurnal tide (Duda and Rainville 2008). Ramp et al. (2004) propose that the strength of internal tides generated in LS may be modulated by the position and strength of the Kuroshio. Stratification in the northern SCS has a strong effect on the propagation of internal tides (Guo et al. 2012; Ramp et al. 2010; Shaw et al. 2009). Results of a recent numerical simulation with idealized initiation parameters indicate that generation of internal tides in LS could be modified by the Kuroshio (Jan et al. 2012). Removing the Kuroshio from the simulation reduces the westward internal tidal energy flux by 30 %, presumably due to weaker stratification at the generation site.

Theoretical and model studies of internal wave propagation through a background flow (Jones 1967; Kunze 1985; Mooers 1975; Olbers 1981; Vlasenko et al. 2005) report that wave propagation is affected by three factors: (1) the Doppler shift, $\omega = \sigma - (\mathrm{K} \cdot \mathrm{U})$, where ω is the intrinsic (Lagrangian) frequency, σ is the Eulerian

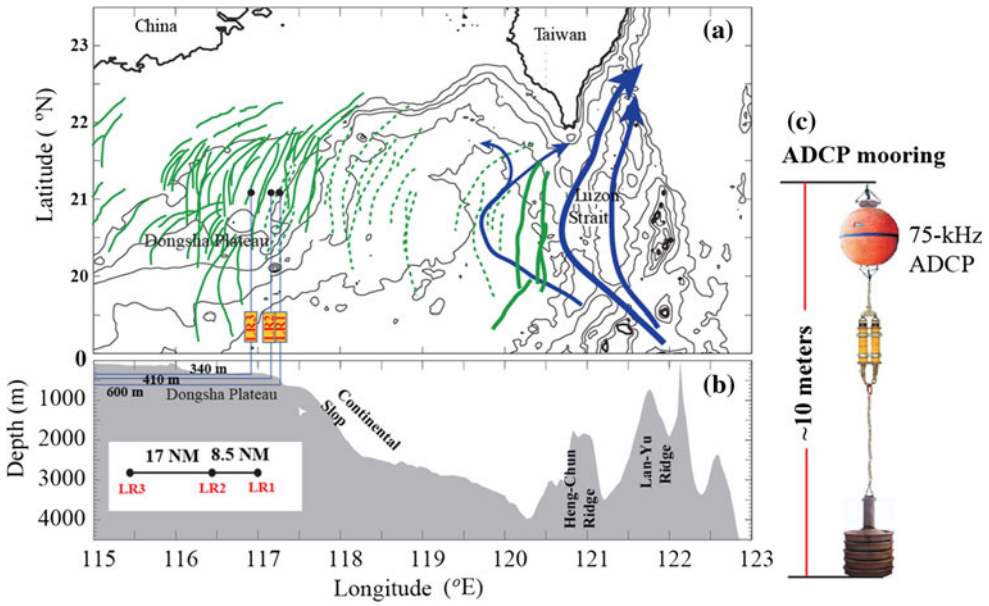

Fig. 1 **a** Map of South China Sea and positions of ADCP moorings (*block dots*). Black contours are 200, 500, 1000, 2000, and 3000 m isobaths. *Green curves* are internal wave packets derived from satellite images by Zhao et al. (2004). *Solid green curves* indicate multiple-wave packets and *dashed green curves* indicate single waves. *Thick solid green curves west of Luzon Strait* represent a big wave event observed on 16 June 1995. *Blue arrows* are the mean paths of Kuroshio current from the NRL model. *Thin blue arrow* is the mean Kuroshio path in October–December 2012. The *thick blue arrow* passing the middle of Luzon Strait is the mean Kuroshio path in June–July 2012. The *thick blue arrow passing east of Luzon Strait* is the mean Kuroshio path in February–May 2013. **b** Bathymetry along 21°N and water depths of ADCP moorings. Horizontal separations between moorings are shown in the *insert*. **c** ADCP mooring configuration. The upward-looking 75 kHz ADCP is mounted at about 10 m above the sea floor

frequency, K = (*k, l, m*) is the wave vector, and U = (*U, V, W*) is the background current; (2) the effective inertial frequency $f_{\text{eff}} = f + \zeta/2 = f + \frac{1}{2}\left(\frac{\partial V}{\partial x} - \frac{\partial U}{\partial y}\right)$, where f is the planetary inertial frequency, U and V are the geostrophic velocities, and $\zeta$is the vertical component of the relative vorticity; and (3) tilting by the horizontal density gradients acting as an additional buoyancy restoring force (Kunze 1985). Interactions between internal waves and the background current have been observed at the North Atlantic subtropical front (Kunze and Sanford 1984), North Atlantic subtropical convergence zone (Lee and Eriksen 1997), California current (Weller 1985), and East China Sea (Rainville and Pinkel 2004). Rainville and Pinkel (2004) report strong Kuroshio vorticity that may affect the propagation behavior of inertial waves and semidiurnal tides in the East China Sea. The strength, position of the Kuroshio, and the stratification associated with the Kuroshio front may have large impacts on the generation, propagation, and dissipation of internal tides in the SCS.

Here we analyze velocity measurements taken from an array of three acoustic Doppler current profiler (ADCP) moorings on the westward propagation path of strong internal tides across the continental slope off Dongsha plateau in the northern SCS. Horizontal kinetic energies in the diurnal and semidiurnal tidal bands show significant intra-annual variability. Results from the Naval Research Laboratory's numerical model, which incorporates the Kuroshio and sub-mesoscale eddies in the SCS with assimilation of satellite altimeter measurements, are used to interpret the observed intra-annual variations of internal tides on the continental slope. The effects of the Kuroshio on internal tidal energy flux are discussed in the context of effective inertial frequency and the vertical and horizontal gradients of horizontal currents. This paper is organized as follows: Sect. 2 describes the observed intra-annual internal tidal energy and Sect. 3 the NRL model and the Kuroshio front. Internal tidal energy flux variations are reported in Sect. 4 and conclusions follow.

2 Internal tide observations

2.1 Mooring description

Three subsurface moorings were deployed in the northern SCS near the Dongsha plateau from June 2006 to May 2007 (Fig. 1). Each mooring was equipped with one upward looking 75 kHz ADCP at 10 m above the sea floor. These ADCP moorings measured three-dimensional velocity over most of the water column at ~340–600 m depth with sampling rates of 60–90 s (Table 1). The moorings were aligned along 21°05′N on the continental slope east of the Dongsha plateau. From east to west, the successive moorings were

Table 1 Mooring locations, measurement periods, water depths, and ADCP sampling configurations

Mooring	Measurement segment	Location	Measurement period	Water depth (m)	Sampling interval (s)	Bin length (m)
LR1	First	21°4.80′N 117°20.75′E	13 Jun–12 Dec 2006	610	90	16
	Second	21°5.26′N 117°20.87′E	14 Jan–7 May 2007	605	90	16
LR2	First	21°4.97′N 117°11.99′E	13 Jun–15 Dec 2006	426	60	8
	Second	21°5.93′N 117°12.32′E	14 Jan–7 May 2007	427	60	8
LR3	First	21°5.43′N 116°54.72′E	13 Jun–26 Sep 2006	367	60	8
	Second	21°5.77′N 116°55.29′E	13 Apr–7 May 2007	342	30	4

separated by ~8.5 nmi (15.7 km) and ~17 nmi (31.5 km), respectively. ADCP velocity measurements taken within 10 % of the ADCP transducer depth beneath the surface, 0–60 m for LR1, 0–42 m for LR2, and 0–34 m for LR3, were contaminated by the surface reflection of ADCP acoustic beams and are not used in this analysis.

2.2 Vertical eigenmode projection

Velocity fluctuations of diurnal tides (D_1) and semidiurnal tides (D_2) are computed from ADCP observations using the second-order Butterworth band-pass filter. The frequency bandwidth for the diurnal tide is $\Delta f(D_1) = [0.71–1.4]$ cycles per day and the frequency bandwidth for the semi-diurnal tide is $\Delta f(D_2) = [1.43–3.3]$ cycles per day. The chosen bandwidth includes the major tidal constituents of K_1, O_1, M_2, and S_2.

To reconstruct the full water column velocity profiles of D_1 and D_2 tidal currents, we apply the vertical eigenmode decomposition (Gill 1982). The non-hydrostatic vertical eigenmode equation is expressed as

$$\frac{\mathrm{d}}{\mathrm{d}z}\left(\frac{1}{N^2}\frac{\mathrm{d}\psi}{\mathrm{d}z}\right) + \frac{1}{(\omega^2 - f^2)/\alpha^2}\psi(z) = 0, \quad (1)$$

where $\Psi(z)$ is the eigenfunction representing the vertical structure of the horizontal current, N is the buoyancy frequency, and α is the magnitude of the horizontal wave number and the eigenvalue is $C_e = (\omega^2 - f^2)/\alpha^2$. $\Psi(z)$ is determined numerically using profiles of $N(z)$. The velocity of the nth eigenmode is computed as

$$u_n(t,z) = u(z,t)[\psi_n(z)]^{-1},\ n = 0,1,2,3,\ldots. \quad (2)$$

At each mooring site, two sources of stratification vertical profiles are used to compute the eigenmodes: (1) the mean $N(z)$ profile taken during the mooring operation cruises and (2) the mean $N(z)$ profile from the climatology dataset provided by the Generalized Digital Environmental Model (GDEM) (Teague et al. 1990) (Fig. 2). Eigenmode vertical structures computed from these two stratification profiles are similar (Fig. 2). The horizontal kinetic energy estimates calculated using both decomposed eigenmodes have similar magnitude. The GDEM profiles for the eigenmode decomposition are used for this analysis because the profiles from the cruises are only available

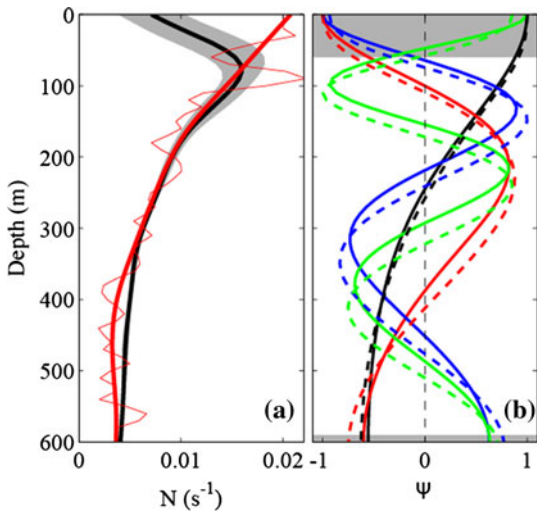

Fig. 2 Vertical profiles of stratification and vertical structure of eigenmodes. **a** Vertical profile of stratification (*thin red curve*) and its low-pass filtered version (*thick red curve*) at LR1 taken during the mooring operation cruise. The *thick black curve* represents the mean vertical profile of stratification provided by the Generalized Digital Environmental Model (GDEM) and the *shading* represents one standard deviation. **b** Vertical structures of the first four baroclinic modes (*black*, *red*, *blue*, and *green curves*) of the horizontal current. *Solid curves* are results computed using the vertical stratification profile obtained during the mooring operation cruise [*thick red curve* in (**a**)] and *dashed curves* are computed using the vertical profile of GDEM [*thick black curve* in (**a**)]. *Horizontal shadings* in (**b**) represent the depth range without velocity observations

Table 2 Percentage of depth integrated horizontal kinetic energy (HKE) of eigenmode of diurnal tide

Moorings	Mode zero (barotropic)	Mode 1	Mode 2	Mode 3	Mode 4
LR1					
HKE_x	16.7	34.0	18.8	20.3	10.2
HKE_y	4.0	42.7	23.0	20.2	10.1
HKE	10.5	38.2	20.8	20.3	10.2
LR2					
HKE_x	27.0	32.5	21.3	11.1	8.2
HKE_y	14.3	43.5	18.7	14.5	9.0
HKE	21.5	37.3	20.1	12.5	8.5
LR3					
HKE_x	22.0	24.4	25.1	17.6	10.9
HKE_y	8.3	31.4	23.7	23.9	12.6
HKE	16.0	27.5	24.5	20.4	11.7

HKE_x and HKE_y are the respective zonal and meridional components of HKE

Table 3 Percentage of depth-integrated horizontal kinetic energy (HKE) of eigenmode of semidiurnal tide

Moorings	Mode zero (barotropic)	Mode 1	Mode 2	Mode 3	Mode 4
LR1					
HKE_x	10.0	55.0	20.1	9.1	5.8
HKE_y	5.1	56.5	17.7	11.7	8.9
HKE	8.2	55.6.	19.2	10.1	7.0
LR2					
HKE_x	7.6	56.3	20.8	10.1	5.3
HKE_y	6.0	50.6	22.4	13.2	7.8
HKE	7.0	54.0	21.4	11.3	6.3
LR3					
HKE_x	10.2	50.6	23.9	10.5	4.7
HKE_y	8.6	42.2	24.8	15.6	8.8
HKE	9.6	47.6	24.2	12.3	6.2

HKE_x and HKE_y are the respective zonal and meridional components of HKE

from the time of the beginning and end of the mooring deployments. Note that the vertical profiles of eigenmode 3 and 4 have their zero crossings close to 60 m depth. Because velocity measurements are not available at depths shallower than 60 m at LR1, projecting observed velocity measurements beyond the 4th eigenmode may introduce errors to the lower modes.

2.3 Horizontal kinetic energy

Horizontal kinetic energy (HKE) is defined as $\rho_o(u^2 + v^2)/2$, where the u and v are the respective zonal and meridional components of velocity. The HKE and its zonal and meridional components of the eigenmode of D_1 and D_2 tides are integrated over the entire water column. For both the D_1 and D_2 tides, the first baroclinic mode has the largest contribution to the HKE, followed by mode 2, mode 3, and the barotropic mode (Tables 2, 3); mode 4 has the smallest contribution. HKE is also computed using the depth compensation method; taking the vertical mean as the barotropic component and computing the residual as the baroclinic component, we then integrate the energy over the ADCP measurement depths. Because ADCP measurements cover about $\sim$90 % of water depth, the HKE is multiplied by a factor of H/h, where H is the water depth and h is the ADCP measurement depth range. Comparing the HKE computed by these two methods for the barotropic D_1 tide at LR1 yields a difference of about 15 % (Fig. 3a). The difference for the baroclinic D_1 HKE is about 10 % (Fig. 3b). The temporal variations in barotropic HKE computed from the two methods are in good agreement. Computations for the D_2 tide yield similar results (not shown).

For this analysis, the baroclinic tides are calculated using the depth compensation method only because limited observed stratification profiles are available and the GDEM monthly climatology may not reflect the stratification during the experiment accurately. The depth-integrated HKE of D_1 is about twice that of D_2. The HKE of D_1 and D_2 decreases from LR1, to LR2, to LR3, suggesting a rapid energy dissipation between LR1 and LR3 (Fig. 4). There is strong intra-annual variability in D_1 at LR1; the highest HKE in July is about twice the mean level. The intra-annual variability is less prominent at LR2 and undetectable at LR3. There is a strong fortnightly cycle of D_1 and D_2 HKE at LR1, but not at LR2 and LR3. Over the transects LR1 to LR2 (8.5 nmi) and LR2 to LR3 (17 nmi), the D_1 and D_2 HKE loses roughly 1/3 to 1/2 of its kinetic energy. The shoaling bottom may have an important role in the energy loss; the internal tide may dissipate energy due to bottom friction or transformation to nonlinear internal waves during the shoaling process (Duda et al. 2004; Holloway et al. 1997; Scotti et al. 2008; Zhao and Alford 2006). Reeder et al. (2011) report very large subaqueous sand dunes and a nepheloid layer near the continental slope resulting from internal wave energy dissipation in the region.

At LR1 and LR2 the weakest and strongest D_1 HKE seasonal averages occur in spring and summer, respectively (Table 4). There is less seasonal variability for D_1 and D_2 tides at LR3. Although HKE is strongest in summer, this is also the season of strongest energy loss as the internal tide propagates westward from LR1 to LR3. We speculate that the stronger stratification during summer has a favorable effect on wave energy propagation across the SCS basin.

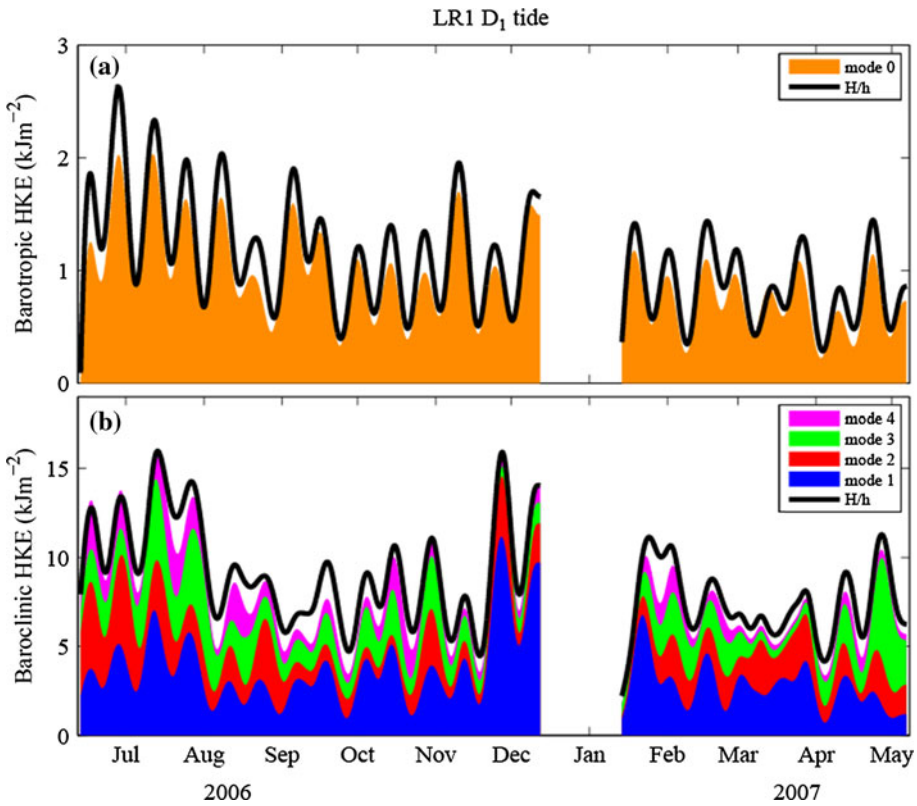

Fig. 3 The horizontal kinetic energy computed using the vertical eigenmode decomposition and depth compensation *H/h* method (Sect. 2.3). **a** The barotropic component. The mode zero in eigenmode decomposition and vertical mean from the data (*black solid line*). **b** The mode 1 (*blue*), sum of modes 1–2 (*red*), 1–3 (*green*), 1–4 (*magenta*), and *H/h* method (*black*). A 7-day low-pass filter has been applied

At LR1, the HKE in December is comparable in amplitude with summer values. At LR2 HKE is greatest in December. This may be attributed to internal tides generated locally; previous studies report that the internal tides may be generated near the continental shelf (Klymak et al. 2011). Our observed HKE amplitudes are 2–3 times those reported by Guo et al. (2012) as expected, because their moorings were located further west in waters 80–250 m deep, where the internal tidal energy is less because a significant fraction of it has been dissipated on the Dongsha plateau (Chang et al. 2006).

3 Internal tide model simulation

3.1 NRL Ocean Nowcast/Forecast model description

The real-time Ocean Nowcast/Forecast System (ONFS) developed at the U.S. Naval Research Laboratory (hereinafter NRL model) is used to interpret the observed variations of internal tidal energy on the Dongsha plateau. The NRL model domain covers the northern SCS, LS, and a portion of the western Pacific with a horizontal resolution of 2.3 km. For vertical resolution, there are 11 terrain-following sigma layers in the top 147 m and 29 isobath layers below. The ONFS system derives its ocean bottom topography from the Digital Bathymetry Data Base in 2 min increments (referred to as DBDS2). Open boundary conditions are derived from a larger scale ONFS for the entire East Asian Sea. The Oregon State University Tidal Prediction Software (OTPS) drives the barotropic tidal currents. A global weather forecast model (Navy Operational Global Atmospheric Prediction System or NOGAPS) and a regional weather forecast model (Coupled Ocean/Atmosphere Mesoscale Prediction System or COAMPS) provide the ocean surface forcing. The ONFS also assimilates satellite altimeter data and multi-channel sea surface temperature (MCSST) from satellite advanced very high resolution radiometer (AVHRR) measurements to further improve model accuracy (Ko et al. 2008).

3.2 Energy flux calculation

The energy flux is a fundamental quantity for understanding internal wave generation, propagation, and dissipation. We script the energy flux of the baroclinic diurnal tide as $F_{\mathrm{bc}-D_1}$ and of the semidiurnal tide as $F_{\mathrm{bc}-D_2}$. The zonal energy flux $F^x = \langle u'p' \rangle$ and meridional energy flux $F^y = \langle v'p' \rangle$ are computed following the method described in Nash et al. (2005). First the density perturbation is computed as

$$\rho'(z,t) = \rho(z,t) - \bar{\rho}(z), \tag{3}$$

where $\rho(z,t)$ is the instantaneous density and $\bar{\rho}(z)$ is the time mean of the vertical density profile. Then the pressure perturbation is derived as

$$p'(z,t) = P_{\text{surf}}(t) + \int_{z}^{0} \rho'(\hat{z},t) g \, \mathrm{d}\hat{z}, \tag{4}$$

where ρ_{surf} is the surface pressure determined by the baroclinicity condition

$$\frac{1}{H} \int_{-H}^{0} p'(z,t) \, \mathrm{d}z = 0. \tag{5}$$

The velocity perturbation is defined by

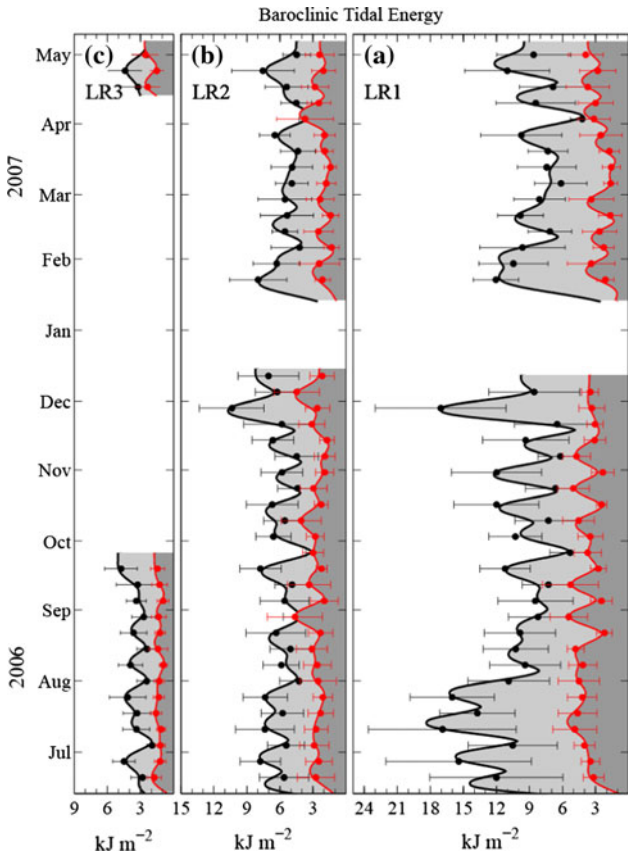

Fig. 4 Horizontal kinetic energy (HKE) of the baroclinic tide at three mooring locations, **a** LR1, **b** LR2, and **c** LR3. *Black lines* indicate diurnal tide (D_1). *Red lines* indicate semidiurnal tide (D_2). The 7 day interval mean and standard deviation of the original series are shown in *black and red dots* and *error bars*

$$u' = u(z,t) - \bar{u}(z) - \bar{u}_o(t), \tag{6}$$

where $u(z,t)$ is the instantaneous velocity, $\bar{u}(z)$ is the time mean, and $\bar{u}_0(t)$ is the depth average of the velocity.

3.3 Strength and position of the Kuroshio during the experiment

The Kuroshio originates from the North Equatorial Current east of the Philippines. As it flows north the Kuroshio enters the SCS from the southern LS, loops around the northern SCS, and exits via the northern LS (Fig. 1a). Kuroshio intrusions are described as intermittent and highly seasonal and favor the generation of large-amplitude internal waves. Though Kuroshio intrusions happen occasionally, it generally does not intrude far into the SCS (Rudnick et al. 2011). The density front of the Kuroshio often hovers near the internal tide generation sites at the east and west LS submarine ridges. The interaction between internal tides and the Kuroshio is thought to be important (Jan et al. 2012). Monthly mean meridional velocity and density contours from NRL model simulations for June 2006–May 2007 along 21°N place the Kuroshio axis ($V > 0.5$ m s^{-1}) near 121°N and about 100 km wide without much variation throughout the period, except during the fall and winter when an intrusion reaches 119°E.

3.4 Internal tide interactions with the Kuroshio density front

Interactions between internal waves and ocean fronts have been observed at the North Atlantic subtropical convergence zone (Lee and Eriksen 1997), East China Sea (Rainville and Pinkel 2004), and South China Sea (Ramp et al. 2004). Rainville and Pinkel (2004) report that the strong background vorticity of the Kuroshio could affect the propagation behavior of semidiurnal tides that encounter Kuroshio fronts in the East China Sea. Kunze (1985) derives a dispersion relation for near-inertial waves

$$\omega_o \approx f_{\text{eff}} + \frac{N^2 k_H^2}{2 f k_z^2} + \frac{g}{\rho f k_z} \left(\frac{\partial \rho}{\partial x} k_x + \frac{\partial \rho}{\partial y} k_y \right) \tag{7}$$

Table 4 Seasonal averages of HKE (kJ m^{-2})

Moorings	Spring (Mar–May)		Summer (Jun–Aug)		Autumn (Sep–Nov)		Winter (Dec–Feb)	
	D_1	D_2	D_1	D_2	D_1	D_2	D_1	D_2
LR1	7.8	2.7	12.3	4.0	9.2	3.6	9.0	2.4
LR2	5.1	2.2	6.1	2.7	6.0	2.6	5.6	2.0
LR3	3.2	2.1	3.2	1.3	3.6	1.3	N/A	N/A

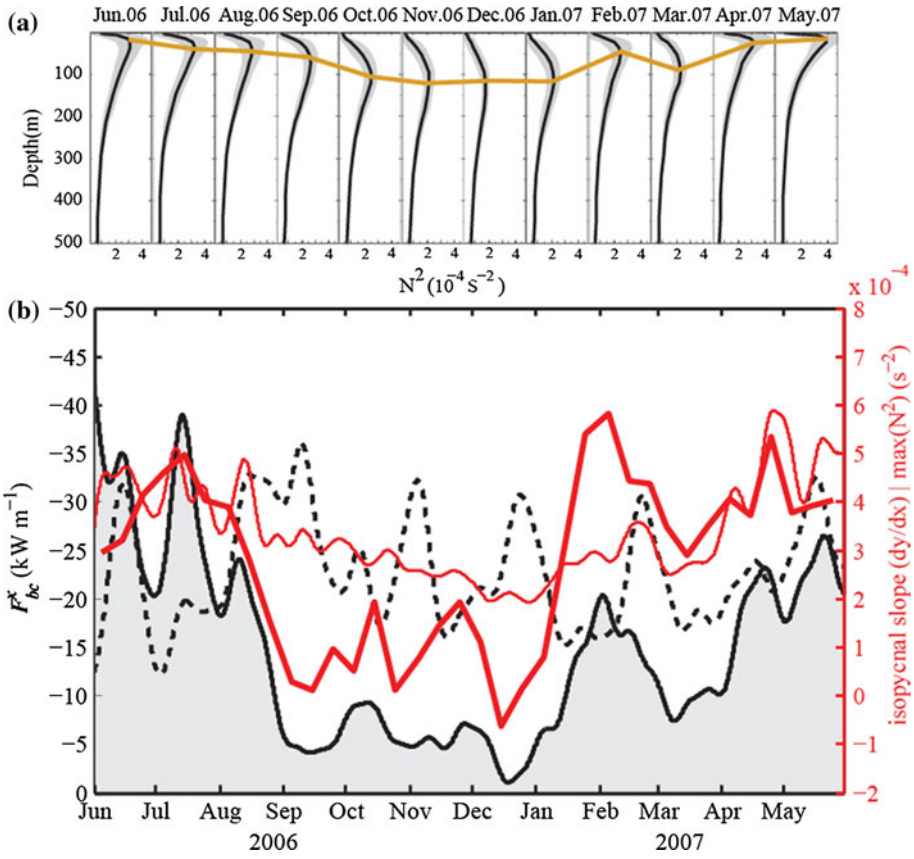

Fig. 5 **a** The monthly mean buoyancy profiles and the depth of maximum stratification (*brown line*). **b** The zonal energy flux and isopycnal slope at 120.5°E 21°N near the internal tide generation site. Black solid line is the D_1 tide depth integrated energy flux ($F^x_{\mathrm{bc}-D_1}$). *Black dashed line* is the D_2 depth integrated energy flux ($F^x_{\mathrm{bc}-D_2}$). The *thick red line* is the isopycnal slope between 120°E and 121°E. The thin red line is the maximum buoyancy frequency squared

and

$$f_{\mathrm{eff}} = \left[f^2 + f\left(\frac{\partial V}{\partial x} - \frac{\partial U}{\partial y}\right) - \frac{\partial V}{\partial x}\frac{\partial U}{\partial y} - \frac{\partial U}{\partial x}\frac{\partial V}{\partial y}\right]^{1/2} \approx f + \frac{1}{2}\left(\frac{\partial V}{\partial x} - \frac{\partial U}{\partial y}\right) = f + \frac{\zeta}{2}, \quad (8)$$

where the ω_o is the intrinsic frequency; N is the buoyancy frequency; f_{eff} is the effective inertial frequency, which equals the planetary value of the inertial frequency f plus half the vertical component of the relative vorticity ζ; $k_H = (k_x^2 + k_y^2)^{1/2}$ is the magnitude of the horizontal wavenumber; $\mathbf{k} = (k_x, k_y, k_z)$ is the wave vector; ρ is water density; and U and V are the background velocities. The dispersion relation is valid for frequencies near or smaller than the effective inertial frequency ($\omega_o < \approx 1.2\ f_{\mathrm{eff}}$). A trapping/amplification in negative vorticity and barrier/reflection in positive vorticity can occur (Kunze 1985). Higher frequency internal waves ($\omega_o \gg f_{\mathrm{eff}}$) are not affected by either rotation or horizontal shear. Rainville and Pinkel (2004) report that the vertical component of geostrophic vorticity associated with the Kuroshio front creates a wall of positive vorticity ($f_{\mathrm{eff}} \approx 2f$) east of Kyushu, which is sufficient to reflect the D_2 tide ($\sim 1.9f$ at 30°N). Calculating the effective inertial frequency at 21°N from the NRL model yields $\omega_o \approx 1.39\ f$ for the D_1 tide and $\omega_o \approx 2.78\ f$ for the D_2 tide. The average value near the Kuroshio front is about 1.1–1.2 f, which is insufficient to change the propagation behavior for either D_1 or D_2 tides.

The vertical shear of the background horizontal current modifies the intrinsic frequency as in Eq. (7), appearing as the horizontal gradient of density according to the thermal wind relation, acting to tilt the particle orbits into the plane of the isopycnals. The particle orbits encounter greater density contrasts on sloping isopycnals than on non-sloped. Comparing the zonal energy flux (F^x_{bc}), isopycnal slope, and monthly mean buoyancy profiles at 120.5°E, 21°N (west of the western ridge) shows that the diurnal energy flux ($F^x_{\mathrm{bc}-D_1}$) is sensitive to the monthly buoyancy profile and the isopycnal slope (Fig. 5). When the Kuroshio occupies the western ridge (Fig. 6a–c, i, k, l), the sloping isopycnals enhance the generation of $F^x_{\mathrm{bc}-D_1}$. The Kuroshio current may modulate the barotropic tidal forcing of internal tide generation. $F^x_{\mathrm{bc}-D_2}$, however, is not affected by the sloping isopycnals near the generation site. The D_2 tide is not generated at this latitude. Previous studies suggest that the two-ridge system in LS dampens or enhances the internal wave amplitude, but this depends on latitude because of the differences in ridge geometry and tidal resonance between ridges (Farmer et al. 2009; Ramp et al. 2012).

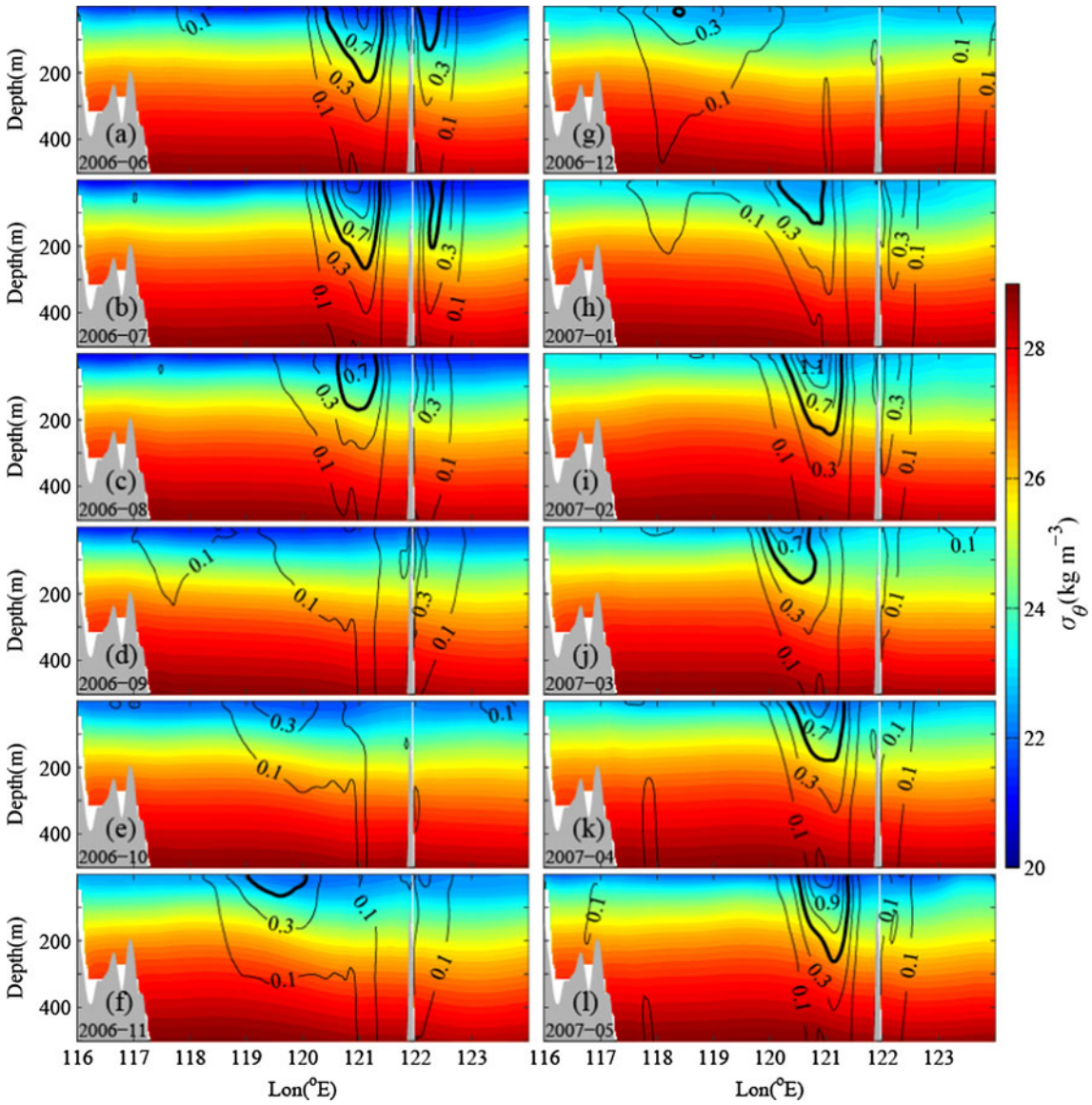

Fig. 6 Monthly density contours and meridional velocity. The *color* background represents the monthly mean density field. The *black contour lines* indicate mean meridional velocity. The *thick black line* is the meridional velocity of 0.5 m s^{-1} contour. The *thin black lines* are velocity contours at 0.2 m s^{-1} intervals

3.5 Energy fluxes across ~21°N

Model simulated energy flux at 21°N, the same latitude as mooring LR1–3, show that negative flux dominates west of LS and positive flux dominates east of LS (Fig. 7). The eastward flux $F^x_{\mathrm{bc}-D_1}$ at 122.5°N (Fig. 7b) matches the barotropic tidal forcing in LS (Fig. 7c). West of the western ridge (Fig. 7d), the $F^x_{\mathrm{bc}-D_1}$ is modified by the presence of the Kuroshio (Sect. 3.4). The stronger $F^x_{\mathrm{bc}-D_1}$ at mid-basin (Fig. 7e) compared with the $F^x_{\mathrm{bc}-D_1}$ west of the western ridge (Fig. 7d) suggests a D_1 tidal beam convergence. The $F^x_{\mathrm{bc}-D_2}$ at 21°N is not affected significantly by either the barotropic tidal forcing or the variation in the Kuroshio front, which indicates that the D_2 tide is not generated at this latitude.

4 Propagation paths of internal tides in the SCS

Propagation path is important to the observed intra-annual variation of internal tidal energy near the Dongsha plateau. The NRL model predictions and observed HKE magnitudes are in agreement, but the modeled and observed time variations in HKE are less well matched. To examine the propagation path, two particular months are selected

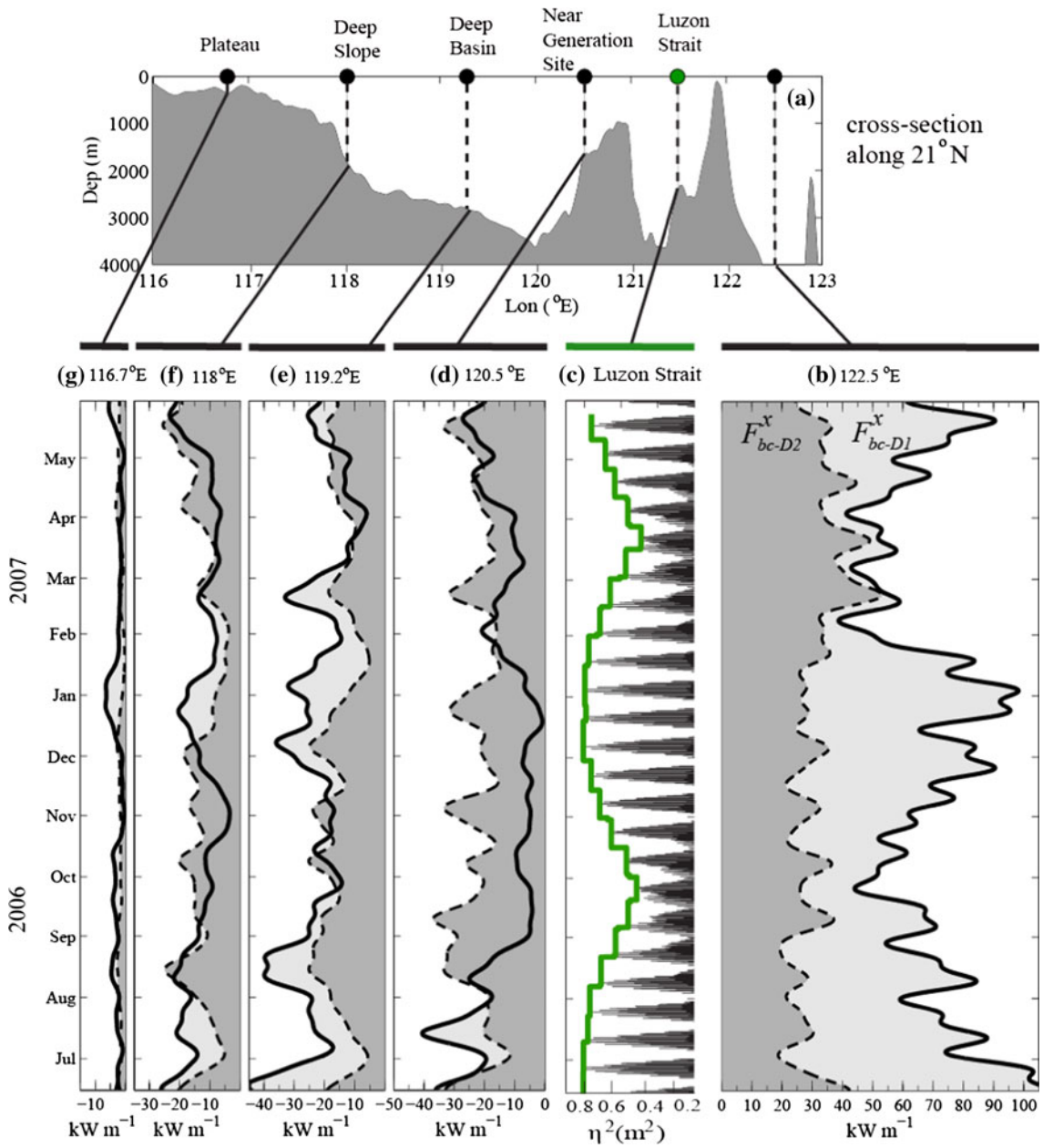

Fig. 7 The cross sections of the time variant $F^x_{\mathrm{bc}-D_1}$ (*solid black lines*) and $F^x_{\mathrm{bc}-D_1}$ (*dashed black lines*) along 21°N at five different longitudes. **a** The bathymetry along 21°N. **b** At 122.5°E, near the internal tide generation site east of the eastern ridge. **c** The barotropic tide at the middle of Luzon Strait from OTPS. The green line is the diurnal frequency envelope. **d** At 120.5°E, near the internal tide generation site west of the western ridge. **e** At 119.2°E, the mid-basin. **f** At 118°E, on the continental slope. **g** At 116.7°E, near the Dongsha plateau, where observational data were collected

(December, Fig. 8a and July, Fig. 8c). Both months have a maximum observed D_1 HKE of $\sim$18 kJ m^{-2} (Fig. 4a). In December the main tidal beam converges and turns southwestward at mid-basin (between 118°E and 119.5°E) and then turns northwest entering the Dongsha plateau (Fig. 8b). A similar propagation pattern is apparent for July (Fig. 8c), but the magnitude is smaller at mid-basin. Over the Dongsha plateau, additional westward flux joins the northwestward flux in December. This may account for the observed stronger HKE in December (Sect. 2.3). Only the northwestward flux propagates toward the Dongsha plateau in July. Mean depth-integrated semidiurnal flux $F_{\mathrm{bc}-D_2}$ in December (Fig. 9a) forms a northwest tidal beam at LS (120°–121°E) and turns westward at 119°E 21°N, toward

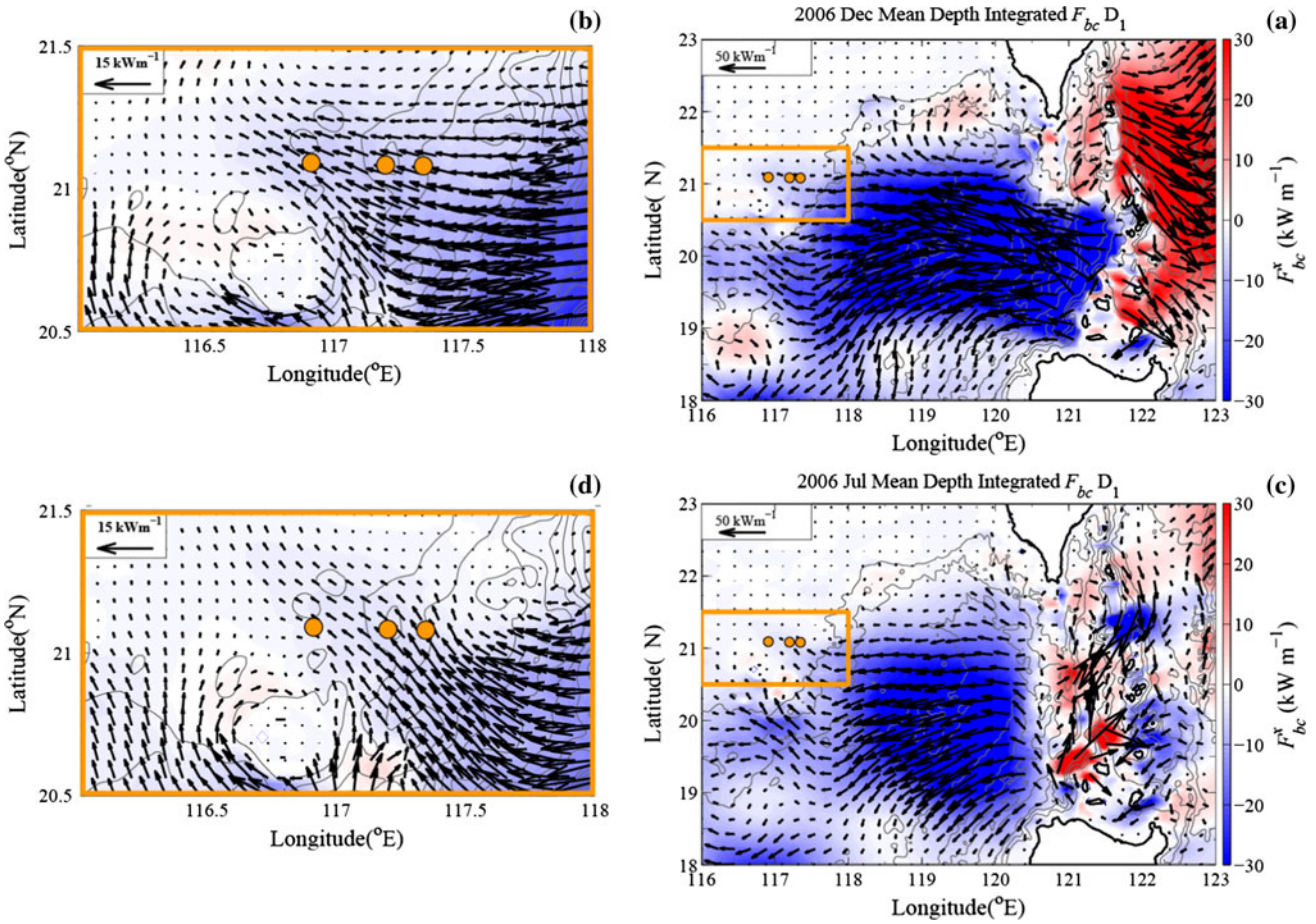

Fig. 8 The depth-integrated diurnal energy flux. The *arrows* represent the vector of $F_{\mathrm{bc}-D_1}$. The *background colors* represent zonal flux $F^x_{\mathrm{bc}-D_1}$: **a** December 2006 and **b** detail of the Dongsha plateau, **c** July 2006 and **d** detail of the Dongsha plateau. The *red dots* indicate mooring LR1–3 locations (as in Fig. 1). The isobath contour interval is 1000 m for (**a**) and (**c**), and 100 m for (**b**) and (**d**)

Dongsha plateau. In July (Fig. 9c), however, multiple generation sites of the depth-integrated semidiurnal flux are apparent in LS, but these fluxes neither join to form the tidal beam nor propagate toward the Dongsha plateau.

5 Conclusions

Three ADCP moorings on the continental slope near the Dongsha plateau of the northern SCS measured the D_1 and D_2 internal tidal energy; the year-long data set reveals strong fortnightly variations. The HKE of the D_1 internal tide is about two times greater than that of the D_2 internal tide. At LR1 and LR2, the weakest and strongest D_1 internal tidal HKE occurs in spring and summer, respectively. At LR3, the shallowest mooring, less seasonal variability was observed for D_1 and D_2 HKE. The energy dissipation as D_1 internal tides propagate westward from LR1 to LR3 is also the greatest in the summer.

The NRL model is used to diagnose internal tide generation and propagation in the northern SCS, with simulations run to coincide with the mooring observation period. The Kuroshio primarily occupies the northern LS near the western ridge, but in the months of September–December it becomes less defined and intrudes into the SCS reaching as far as 119°E. The Kuroshio enhances the generation of D_1 tidal energy near the generation site due to the increases in stratification and isopycnal slope. The vertical relative vorticity that modulates the effective inertial frequency (1.1–1.2 f), however, is not sufficient to modify the propagation behavior of either the D_1 ($\omega_o \approx 1.39\ f$) or D_2 ($\omega_o \approx 2.78\ f$) tide at 21°N. Although the Kuroshio modifies D_1 tidal generation at LS, the observed large intra-seasonal variation in the tidal energy flux on the Dongsha plateau is due mainly to the variation in the tidal beam propagation in

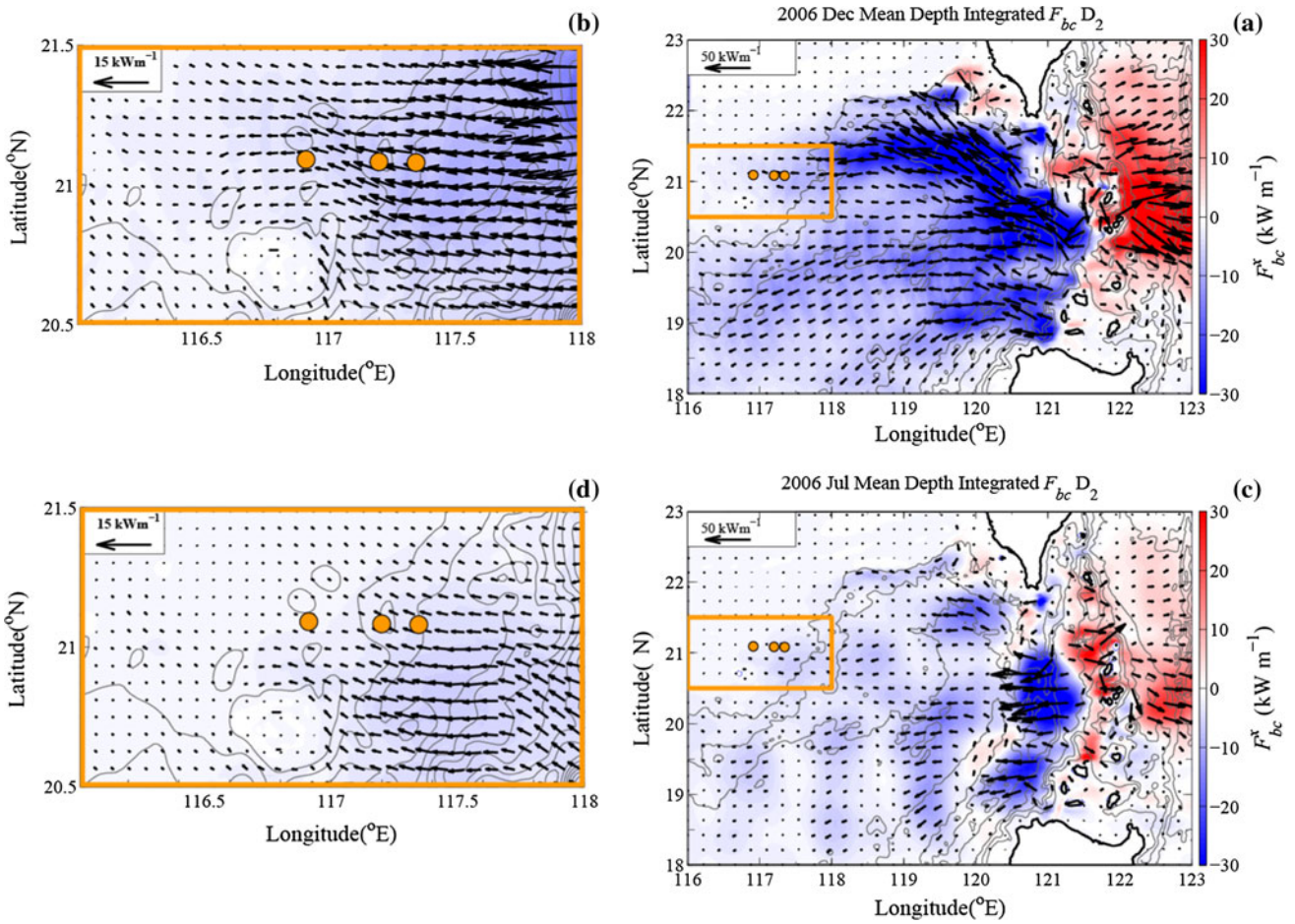

Fig. 9 The depth-integrated semidiurnal energy flux. The *arrows* represent the vector of $F_{\mathrm{bc}-D_2}$. The *background colors* represent zonal flux $F^x_{\mathrm{bc}-D_2}$: **a** December 2006 and **b** detail of the Dongsha plateau, **c** July 2006 and **d** detail of the Dongsha plateau. The *red dots* indicate mooring LR1–3 locations (as in Fig. 1). The isobath contour interval is 1000 m for (**a**) and (**c**), and 100 m for (**b**) and (**d**)

the deep basin between LS and the plateau. Stratification influences the tidal beam's propagation path and, therefore, the energy flux on the Dongsha plateau.

Acknowledgments The authors thank the captain and crew of the R/V *Ocean Researcher I* and R/V *Ocean Researcher III*, and Mr. Wen-Hwa Her of the National Taiwan University for their skillful mooring operations. Discussions with Frank Henyey, Eric D'Asaro, and Eric Kunze are greatly appreciated. The comments from two anonymous reviewers helped greatly to improve the presentation of the manuscript. The experiment and analysis are supported by the U.S. Office of Naval Research grant N00014-09-1-0279. DSK is supported under grant N00014-05WX-2-0647.

References

Chang MH, Lien RC, Tang TY, D'Asaro EA, Yang YJ (2006) Energy flux of nonlinear internal waves in northern South China Sea. Geophys Res Lett 33. doi:10.1029/2005GL025196

Duda TF, Rainville L (2008) Diurnal and semidiurnal internal tide energy flux at a continental slope in the South China Sea. J Geophys Res 113. doi:10.1029/2007JC004418

Duda TF, Lynch JF, Irish JD, Beardsley RC, Ramp SR, Chiu CS, Tang TY, Yang YJ (2004) Internal tide and nonlinear internal wave behavior at the continental slope in the northern South China Sea. IEEE J Ocean Eng 29:1105–1130

Farmer D, Li Q, Park JH (2009) Internal wave observations in the South China Sea: the role of rotation and non-linearity. Atmos Ocean 47:267–280

Gill AE (1982) Atmosphere-ocean dynamics. Academic Press, New York, p 662

Guo P, Fang WD, Liu CJ, Qiu FW (2012) Seasonal characteristics of internal tides on the continental shelf in the northern South China Sea. J Geophys Res 117. doi:10.1029/2011JC007215

Holloway PE, Pelinovsky E, Talipova T, Barnes B (1997) A nonlinear model of internal tide transformation on the Australian North West Shelf. J Phys Oceanogr 27:871–896

Jan S, Chern CS, Wang J, Chiou MD (2012) Generation and propagation of baroclinic tides modified by the Kuroshio in the Luzon Strait. J Geophys Res 117. doi:10.1029/2011JC007229

Jones WL (1967) Propagation of internal gravity waves in fluids with shear flow and rotation. J Fluid Mech 30:439–448

Klymak JM, Alford MH, Pinkel R, Lien R-C, Yang YJ, Tang TY (2011) The breaking and scattering of the internal tide on a continental slope. J Phys Oceanogr 41(5):926–945

Ko DS, Martin PJ, Rowley CD, Preller RH (2008) A real-time coastal ocean prediction experiment for MREA04. J Mar Syst 69(1–2):17–28

Kunze E (1985) Near-inertial wave propagation in geostrophic shear. J Phys Oceanogr 15(5):544–565

Kunze E, Sanford TB (1984) Observations of near-inertial waves in a front. J Phys Oceanogr 14(3):566–581

Lee CM, Eriksen CC (1997) Near-inertial internal wave interactions with mesoscale fronts: observations and models. J Geophys Res 102(C2):3237–3253

Lee IH, Wang YH, Yang Y, Wang DP (2012) Temporal variability of internal tides in the northeast South China Sea. J Geophys Res Oceans 117. doi:10.1029/2011JC007518

Mooers CNK (1975) Several effects of a baroclinic current on the three-dimensional propagation of inertial-internal waves. Geophys Fluid Dyn 6:277–284

Nash JD, Alford MH, Kunze E (2005) Estimating internal wave energy fluxes in the ocean. J Atmos Ocean Technol 22(10):1551–1570

Olbers DJ (1981) The propagation of internal waves in a geostrophic current. J Phys Oceanogr 11(9):1224–1233

Rainville L, Pinkel R (2004) Observations of energetic high-wavenumber internal waves in the Kuroshio. J Phys Oceanogr 34(7):1495–1505

Ramp SR, Tang TY, Duda TF, Lynch JF, Liu AK, Chiu CS, Bahr FL, Kim HR, Yang YJ (2004) Internal solitons in the northeastern South China Sea—part I: sources and deep water propagation. IEEE J Ocean Eng 29(4):1157–1181

Ramp SR, Yang YJ, Bahr FL (2010) Characterizing the nonlinear internal wave climate in the northeastern South China Sea. Nonlinear Proc Geophys 17(5):481–498

Ramp SR, Yang YJ, Reeder DB, Bahr FL (2012) Observations of a mode-2 nonlinear internal wave on the northern Heng-Chun Ridge south of Taiwan. J Geophys Res 117. doi:10.1029/2011JC007662

Reeder DB, Ma BB, Yang YJ (2011) Very large subaqueous sand dunes on the upper continental slope in the South China Sea generated by episodic, shoaling deep-water internal solitary waves. Mar Geol 279(1–4):12–18

Rudnick DL, Jan S, Centurioni L, Lee CM, Lien R-C, Wang J, Lee D-K, Tseng R-S, Kim YY, Chern C-S (2011) Seasonal and mesoscale variability of the Kuroshio near its origin. Oceanography 24(4):52–63

Scotti A, Beardsley RC, Butman B, Pineda J (2008) Shoaling of nonlinear internal waves in Massachusetts Bay. J Geophys Res 113. doi:10.1029/2008JC004726

Shaw PT, Ko DS, Chao SY (2009) Internal solitary waves induced by flow over a ridge: with applications to the northern South China Sea. J Geophys Res 114. doi:10.1029/2008JC005007

Teague WJ, Carron MJ, Hogan PJ (1990) A comparison between the generalized digital environmental-model and levitus climatologies. J Geophys Res 95:7167–7183

Vlasenko V, Stashchuk N, Hutter K (2005) Baroclinic tide: theoretical modeling and observational evidence. Cambridge University Press, Cambridge, p 351

Weller RA (1985) Near-surface velocity variability at inertial and subinertial frequencies in the vicinity of the California current. J Phys Oceanogr 15(4):372–385

Zhao ZX, Alford MH (2006) Source and propagation of internal solitary waves in the northeastern South China Sea. J Geophys Res 111. doi:10.1029/2006JC003644

Zhao Z, Klemas V, Zheng Q, and Yan X-H (2004) Remote sensing evidence for baroclinic tide origin of internal solitary waves in the northwestern South China Sea. Geophys Res Lett 31. doi:10.1029/2003GL019077